

A piezoelectric ski-jump laser beam scanning chip-to-free space photonic link

Matt Saha^{*,1,α}, Y. Henry Wen,^{*,1,β} Andrew S. Greenspon^{*,1,2,γ}, Matthew Zimmermann¹, Kevin J. Palm¹, Alex Witte¹, Mark Dong^{1,2}, Andrew J. Leenheer³, Genevieve Clark^{1,2}, Gerald Gilbert^{4,*}, Matt Eichenfield^{3,5,ε}, and Dirk Englund^{2,†}

**These authors contributed equally to this work.*

¹The MITRE Corporation, 202 Burlington Road, Bedford, Massachusetts 01730, USA

²Research Laboratory of Electronics, Massachusetts Institute of Technology, Cambridge, Massachusetts 02139, USA

³Sandia National Laboratories, P.O. Box 5800 Albuquerque, New Mexico 87185, USA

⁴The MITRE Corporation, 200 Forrestal Road, Princeton, New Jersey 08540, USA

⁵College of Optical Sciences, University of Arizona, Tucson, Arizona 85719, USA

^αmsaha@mitre.org, ^βhwen@mitre.org, ^γagreenspon@mitre.org,

^{*}ggilbert@mitre.org, ^εeichenfield@arizona.edu, [†]englund@mit.edu

©2024 The MITRE Corporation. ALL RIGHTS RESERVED

Summary

A seamless interface between integrated photonic processors and targets in free-space enables wide-ranging advancements in telescopy, free-space communication, optical ranging, materials processing, biomedical imaging, near eye display, machine optical intelligence and quantum control. An optimal solution allows for 2D scanning from anywhere on a photonic chip over a large number of diffraction limited spots in the far field. Leading approaches rely on scanners where the numerical aperture and actuator size are linked, resulting in a trade off between resolution, speed and footprint, whereas scanning fibers have been limited to bulk optical and mechanical components. Here, we introduce a CMOS fabricated photonic “ski-jump” composed of a broadband, single mode silicon nitride waveguide monolithically integrated atop a piezo-actuated cantilever. The ski-jump passively curl 90° out-of-plane via mechanical meta-stress engineering in a footprint of less than 0.1 mm² and emit submicron diffraction-limited optical modes with piezoelectric steering. They also exhibit kHz-rate longitudinal and lateral mechanical resonances with displacement ranges exceeding 400 μm and 180 μm, respectively, and quality factors $Q > 10,000$ under vacuum. These resonances enable 2D beam scanning at footprint-adjusted spot-rates of 68.6 Megaspot/s-mm² surpassing state-of-the-art MEMS mirrors by more than 50×. Using these devices, we demonstrate arbitrary 2D image projection and the repeatable initialization and readout of single photons from silicon vacancies in diamond waveguides. Based on current device performance, we identify pathways for achieving >1 Giga-spots in a cm² area to provide a seamless, scalable optical pipeline between integrated photonic processors and the free-space world.

Introduction

The information content of our world, from the astronomically large to the quantum mechanically small, is predominantly photonic. The ability to project and collect light over many free-space modes at visible-NIR wavelengths opens up exciting opportunities across the areas of astronomy^{1,2}, free-space communications^{3,4}, light detection and ranging (LiDAR)⁵⁻⁷, materials processing⁸⁻¹⁰, near-eye displays¹¹⁻¹³, neuroscience^{14,15}, machine-learning acceleration¹⁶⁻²¹, and atom control for quantum information^{22,23}. However, our current digital infrastructure struggles with the immense data streams coming from real-world, free-space domains where every resolvable pixel is potentially a separate channel that must be received, understood, and acted upon^{22,24}. As digital intelligent systems become more capable, the chip-to-free-space optical interface becomes a crucial link in the digital intelligence value chain. Concurrently, integrated photonic circuits have advanced beyond basic modulation and detection schemes^{25,26} towards increasingly sophisticated functionalities: complex light conditioning for the control of atomic arrays and free-space displays^{7,23,24}, in-physics algorithms, and deep co-learning at the edge^{12,25-28}.

Despite this, the lack of a mode-efficient interface between the guided-wave mode-space of photonic integrated circuits (PICs) and the continuous mode-space of free-space domains has prevented the seamless and scalable application of PICs in many of these areas. Integrated waveguide systems have a large number of time-bin modes by virtue of the >100 GHz-rate electro-optic modulation and THz-rate all-optical interactions but are practically limited by the number of spatial waveguides per chip (100-1000/mm) with diffraction-limited input/output (I/O) available only at the chip edge. In contrast, the free-space domain has a nearly unbounded number of spatial modes ($\sim 10^{12}/\text{m}^2$) with relatively slow temporal variations ($< 10^3$ - 10^6 Hz) for many relevant applications^{7,11,27,28}. Despite the total mode count being similar ($\sim 10^{15}$ - 10^{18}), existing solutions fail to bridge this mode-space mismatch due to 1) poor aperture fill-factor²⁹⁻³¹, 2) limited field of view (FoV) or 3) lack of direct, scalable coupling into PICs^{7,11,28,32-38}, with no clear path to overcoming these limitations. Tiled aperture devices such as spatial light modulators (SLM) and digital mirror displays (DMD) offer a large array of individually controlled pixels capable of generating highly structured light at moderate speeds^{39,40}, but the discontinuous aperture leads to diffractive features in the far field. While recent advances in SLMs⁴¹⁻⁴⁴ seek to overcome these challenges, limited FoV and lack of direct PIC integration remain open challenges. Devices with native PIC integration require diffractive gratings to emit light out-of-plane from the chip surface^{29,31}, limiting both the near-field fill-factor and far-field spatial resolution while also suffering from transmission losses to other diffractive orders and/or restrictions on optical bandwidth and polarization.

Alternatively, continuous aperture laser beam scanners^{7,32,33} have, by construction, a fully-filled aperture in the case of pupil plane scanners (MEMS mirrors, AODs) or emit a waveguide mode in the case of focal plane scanners (scanning fibers or waveguides). This enables them to project and scan a single diffraction limited beam spot to the far-field, but with limited scalability. Fig. 1a compares the performance of leading laser beam scanning technologies as a function of the 1) footprint adjusted pixel count and 2) the refresh rate

calculated using the expressions in Supplementary Section 8. Together these compose the net figure of merit (FoM): spots/s-mm². This value quantifies how many resolvable beam-spots can be accessed in one second from a 1 mm² device area and allows the direct comparison of pupil plane and focal plane scanners without regard to whether the scanning DoF is angular or displacement (Fig 1a, lower left). Pupil plane scanners (AODs, MEMs mirrors) scan a collimated beam in angular degrees-of-freedom (DoF) and require a larger aperture to achieve a lower divergence beam and therefore tighter resolution in the far field. This creates a fundamental trade-off due to the slower rate of modulation of larger apertures. This limit is set by the access time for AODs, i.e. the time it takes for a sound wave to traverse the beam width; and by the mechanical resonance of the mirror aperture for MEMs mirrors, i.e. a smaller mirror can move faster by virtue of higher resonance frequencies but has lower far-field resolution due to the larger divergence of a smaller aperture. The mirror diameter also needs to be larger than the beam waist by at least a factor of 3 at all angles, incurring a $3\cos(\theta_{scan}/2)$ penalty in order to avoid Airy diffraction. The upper bound near 500K and 1M spots/s-mm² for AODs and MEMS mirrors, respectively, reflects this fundamental trade-off. However, regardless of the scanning FoM, none of these directly couples to a PIC without additional free-space micro-optical elements, rendering them practically unscalable to the mode counts required for full spatio-temporal projection and collection.

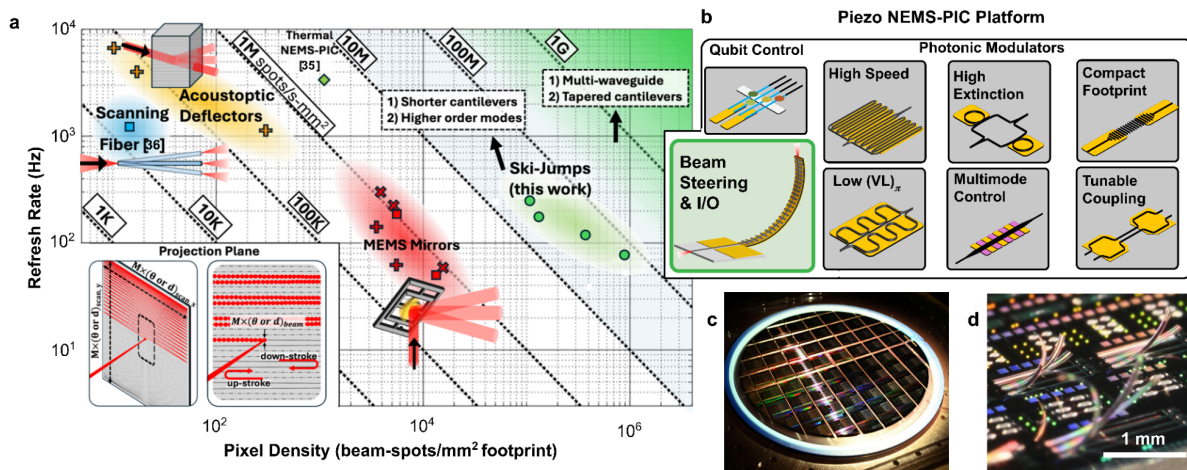


Fig. 1 | Comparison of photonic ski-jump with other beam steering technologies and overview of the underlying NEMS-PIC platform. a, Comparison of photonics ski-jump with leading laser beam scanning performance as a function of footprint adjusted pixel density and refresh rate. Each decade of the net FoM, spots/s-mm², is marked. data points (green circles) are obtained from a single device measured in vacuum (< 0.1 mTorr) at peak-to-peak voltages (V pk-pk) of 1, 2, 5, and 10 (left to right). (Lower left inset) Projection plane FoV is given by the scan angle for pupil plane scanners or scan distance for focal plane scanners scaled by magnification M. References are given in figure for scanning fiber and thermal NEMS-PIC. AODs data points are from refs. ⁴⁵⁻⁴⁷, MEMS mirrors data points are from table in ref.⁷. **b,** Underlying piezo-actuated NEMS-PIC platform with family of modulators, couplers and qubit control sockets on a single monolithic wafer. From top left to bottom right: Strain solid-state qubit control⁴⁸, and optical modulators with various capabilities: (top row) 100 MHz bandwidth⁴⁹, greater than 40 dB extinction²³, strain-concentrated for compact footprint (<0.003 mm²)⁵⁰, bottom row: (this work) ski-jump for beam steering and I/O, sub 10 V-cm (VL) π ⁵¹, programmable multimode interferometer⁵², tunable-gap directional coupler ⁵³. **c,** A diced, unreleased NEMS-PIC wafer. **d,** Various ski-jump device designs on a released NEMS-PIC chip.

Focal plane scanners, such as scanning fibers and waveguides, scan a waveguide mode in both angular and displacement DoFs. These provide a potentially powerful alternative to pupil

plane scanners since 1) the numerical aperture and actuator size are not fundamentally linked, and 2) they are naturally implemented in waveguides which couple directly between the guided-wave mode space and the free-space mode space^{37,54}. Single scanning fibers have been functionalized for endoscopy^{55,56} with the refresh rates potentially comparable to MEMS mirrors³⁷, and have been intensely pursued as a candidate for near-eye displays.^{13,57-59} However, development in this area has been limited to the use of bulk fibers and actuators³⁷ resulting in $>100 \text{ mm}^2$ footprint, large spot size, and an FoM below 10 Kspots/s-mm^2 . It is therefore clear that this approach has been impeded by the lack of a scalable and monolithic fabrication process for scanning nano-scale, high-NA, single mode waveguides with direct and flexible coupling to a PIC platform. Azadeh *et. al.* sought to overcome these limitations using thermally actuated waveguide-on-NEMS cantilever and achieved a $2\times$ FoM improvement over leading MEMS mirrors. But the inability to achieve vertical diffraction-limited emission and weak thermal actuation limited the far field beam-spot density, FoV, speed and power efficiency compared to piezo-actuated PICs^{49,51,60}.

Here, we overcome these challenges by fabricating photonic s, a nanoscale photonic waveguide embedded on a piezo-actuated microcantilever with large out-of-plane curvature. This enables vertical emission from anywhere on a 200 mm complementary metal-oxide-semiconductor (CMOS) wafer, achieving a $1000\times$ FoM improvement over existing fiber scanning demonstrations and a $50\times$ FoM improvement over mature MEMS mirror solutions^{49,60} without active stabilization. The large upward curvature is achieved via a mechanical metamaterials approach to engineer the directionality of the intrinsic material stress differential between the thin film layers of the cantilever. This results in vertical orientation of the waveguide tip due to passive stress alone for cantilevers with lengths less than 1 mm without the need for annealing, ion-implantation, or additional post-processing. Ski-jumps also exhibit mechanical resonances from $\sim 1 \text{ kHz}$ to $>100 \text{ kHz}$ that significantly enhance the speed and FoV over which the waveguide output scans. The result is actuatable, optically broadband waveguides that emit light vertically from the plane of the PIC for routing and steering of light off-chip.

Photonic ski-jumps exist within a unified family of piezo-actuated components on a 200 mm , CMOS-compatible nanoelectromechanical systems of photonic integrated circuits (NEMS-PIC) platform (Fig. 1b); these includes: tunable and non-tunable directional couplers⁵³, strain-optic and cantilever-based phase shifters^{49,60}, Mach Zehnder interferometers^{51,17}, programmable multimode interferometers⁶¹, wavelength-tunable ring resonators^{23,60}, and polarization splitters and rotators⁶². These allow 100 MHz -rate on-chip modulation, polarization and optical mode control, wavelength multiplexing, and phase control upstream of the scanner. Ski-jumps are also cryogenically compatible, and compatible with heterogeneous integration of diamond microchips with single-photon emitters and strain-tunable color centers^{48,63}, opening up new routes for addressing and readout of spin qubits. GHz-rate resonant modulation has been demonstrated with photonic crystal cavity modulators⁵⁰, and 100 GHz modulation has been demonstrated on silicon nitride (SiN) using thin film lithium niobate⁶⁴. This would allow for the

projection of sub-nanosecond optical pulses. Using this extensive library of devices as a process development kit (PDK) enables photon control on- and off-chip.

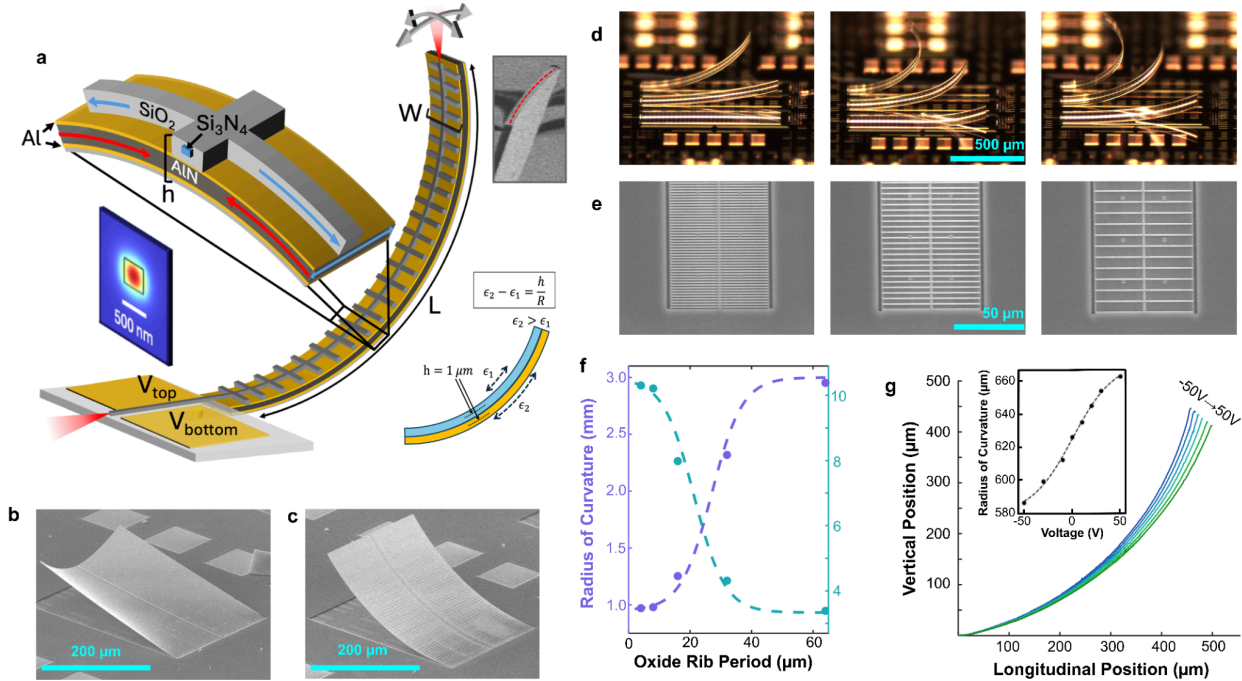


Fig. 2 | Overview of the photonic ski-jump device. **a**, Conceptual overview. Zoomed-in segment shows the cross-section composed of the lower piezo layers (SiO₂-Al-AIN-Al) and upper optical layers SiN-in-SiO₂. Each set of layers is ~1 μm thick resulting in a ~2 μm thick cantilever. Large curvature is obtained using cross-rib patterning of top oxide which expands laterally (blue arrows), leading to downward lateral curvature and lateral compression (red) and longitudinal expansion (blue) of lower layers, ultimately leading to upward curvature. The downward lateral curvature is observed via SEM (upper right inset). An FEM simulation of the TE single mode profile along the waveguide operating at 737 nm using a 400 nm wide and 300 nm thick waveguide is included (lower left inset), along with a conceptual diagram of differential strain between the top and bottom layers (lower right inset). **b-c**, comparison of cantilever without (b) and with (c) cross-ribs to suppress lateral upward curvature and enhance longitudinal curvature. **d**, Variation of curvature with cross-rib period, width, waveguide count. From top to bottom in each subpanel, the cantilevers are 70 μm, 90 μm, and 110 μm wide with 1, 2 and 4 SiN waveguides spaced 3 μm apart along the midline of the cantilever. Cross-ribs are all 0.75 μm wide with a pitch of (left) 2 μm, (middle) 4 μm, or (right) 8 μm. **f**, Curvature for cross-rib period from 4 to 64 μm showing an optimum between 4-8 μm. **g**, DC actuation measured using white-light profilometry for -50 V to 50 V, (inset) radius of curvature for each dataset as a function of the applied DC voltage.

In this paper, we first provide an overview of the device design and methods for optimizing the passive curvature of the cantilever, followed by optical and electromechanical characterization for the device. We show broadband optical transmission, longitudinal DC scanning, AC scanning in both longitudinal and lateral directions with an analysis of the mechanical mode spectrum at various levels of vacuum and at cryogenic temperature. We then provide two proof-of-principle demonstrations. First, by using a split-electrode device and driving lateral and longitudinal resonances simultaneously with phase control, we drive a variety of 2D scan patterns and demonstrate arbitrary image projection using synchronized optical modulation. We then demonstrate on-resonant excitation of single and ensemble silicon vacancy (SiV) color centers in a diamond microchiplet using optical excitation from a ski-jump device. Finally, we draw up a blueprint for a beam steering array with >1 Giga-spot from less than 1 cm² of chip area, enabling a seamless optical pipeline between photonic processors and the free-space world.

Device overview

Photonic ski-jump are fabricated using a 200 mm CMOS foundry process which incorporates an undercut aluminum nitride (AlN) piezo-actuator layer. Voltage is applied across the top and bottom metal electrodes surrounding the AlN to induce piezoelectric stress which in turn produces deflection of the cantilever. SiN waveguides, cladded in SiO₂, are patterned at the top of the layer stack⁴⁹. These waveguide dimensions can be tailored for broadband, single mode (SM) or multimode (MM) propagation of the desired polarization. The devices studied here have 400 nm wide x 300 nm thick waveguides optimized for single mode propagation at 737nm, as shown in the mode profile included in Fig 2a. The waveguide width can also be tapered near the cantilever tip to achieve the desired output spot size and beam divergence.

The materials forming the device each have varying levels of compressive intrinsic stress, that is, expansion upon release from the substrate which results in cantilever curvature based on the bimorph mechanism⁶⁵ (Fig. 2a). This curvature can be varied by modifying the geometry of the device, notably the cantilever length (L), cantilever width (W), number of waveguides on the device (wgN), and the SiO₂ pattern above the top electrode. A fully-filled top oxide layer results in strong downward curvature, whereas removing all oxide except for the cladding region results in weak upward curvature. Noting that the intrinsic stress is isotropic, we develop a method to structurally modify the directionality of the film stress gradient in order to suppress the lateral curvature and enhance the longitudinal curvature. We achieve this by patterning the top silicon dioxide (SiO₂) into periodic lateral rib structures which has two key effects: 1) the compressive stress of the waveguide is evenly spread across the entire width of the cantilever while not contributing additional compressive longitudinal stress from the top-oxide layer, and 2) the bottom layers are laterally compressed leading to further longitudinal expansion and upward curvature. The strength of the cross-rib mechanism is adjusted by changing the cross-rib period and duty cycle, as shown in Fig. 2b-f, with an optimum between 4 μm to 8 μm. Finite element method (FEM) simulation also confirms the qualitative curvature enhancement of a cross-rib pattern.

Characterization of ski-jump cantilevers

DC actuation can tune the angle and position of the ski-jump's optical output, serving as a useful tool for optimizing coupling to free-space optics, optical fibers, directly to free-space targets, or to other PICs. DC actuation for a device was characterized using a white light profilometer (Fig. 2g). This device (L=800 μm, W=90 μm, passive deflection of 70.2°) demonstrated an angular range of 8.5°, a vertical displacement range of 34.4 μm, and a longitudinal displacement range of 29.4 μm for DC voltages of -50 V to 50 V. Each device also exhibits mechanical resonances that substantially enhance AC actuation of the cantilever. The resonance frequencies and mode shapes are determined by the material stresses, stiffnesses, and the device geometry; particularly, cantilever length and the thickness in the bending direction⁶⁶. Mechanical eigenmodes are simulated using FEM (Fig. 3a) and agree with the characteristic

modes of a singly clamped cantilever with a passive curvature. The majority of resonances within the simulated frequency range are longitudinal since the bending dimension is the film thickness. For lateral modes, the bending dimension is the cantilever width which produces a higher effective stiffness. Unlike pupil plane scanners which scan the angle of the beam, focal plane scanners scan both the angle and displacement depending on the trajectory of the excited modes.

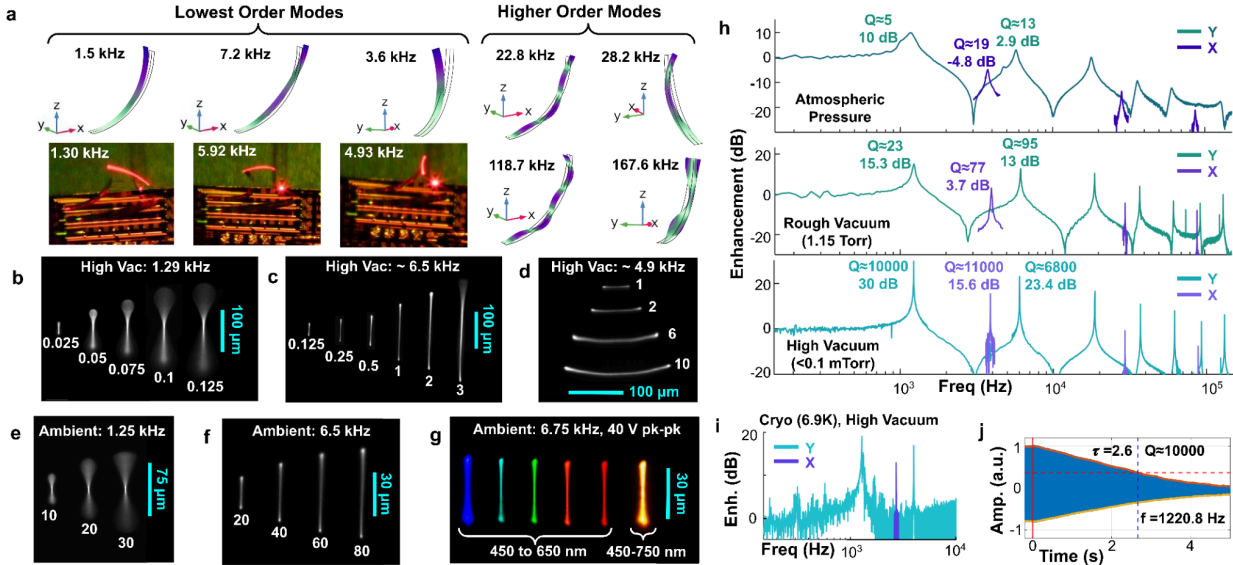


Fig. 3 | Characterization of mechanical resonance modes. **a**, FEM simulations for 7 of the resonant modes for a curled cantilever ($L=950 \mu\text{m}$, $W=70 \mu\text{m}$). Below: Images of a resonantly driven cantilever at its first two longitudinal modes and first lateral mode. **b-f**, ICCD images of the waveguide output on resonance with various drive voltages (streak labels in units V pk-pk) for a device with dimensions: $L = 950 \mu\text{m}$, $W = 70 \mu\text{m}$. The exposure time is greater than the drive signal period so that the full range of motion is observed. Subpanels show the first two longitudinal modes and the first lateral mode in ambient and/or in high vacuum conditions. **g**, Broadband operation is demonstrated on a different device ($L=950 \mu\text{m}$, $W=90 \mu\text{m}$) with a second-order longitudinal mode at 6.75 kHz. **h**, Small signal frequency response of the longitudinal and lateral beam displacement for the device used in (b-f). Measurements were taken with the device at atmospheric pressure, rough vacuum, high vacuum, and **i**, cryogenic conditions at high vacuum. Data is normalized to the Y displacement at low frequencies. **g**, Ring-down measurement for the fundamental longitudinal mode in high vacuum.

We characterize the AC response of a device at various pressures and at 6.9 K. The waveguide output is collected using an objective and imaged onto a CMOS camera, an intensified charge coupled device (ICCD), or a position sensitive photodetector (PSD), with further experimental setup details provided in Supplementary Section 3. These devices were driven with sinusoidal voltages with amplitudes up to 80 V pk-pk. The motion of the cantilever is predominantly in Y for the longitudinal modes and in X for the lateral modes. These modes also have varying degrees of out of plane (Z) motion, depending on the mechanical mode profile. The fundamental mode profile moves nearly along a circular arc for tip angles less than 90° and exhibits equal Y and Z motion ($> 400 \mu\text{m}$) in this range and $> 90^\circ$ of angular range, as shown in stroboscopic imaging of the resonance mode profile (Supplementary Video 6) and in the defocusing of the beam in the ICCD images (Fig. 3b, 3e). In contrast, the higher order modes and notably the 2nd order Y mode, exhibit much lower Z and angular motion due to the additional motional nodes. This separates the cantilever into distinct segments with opposing changes in curvature such that the composite motion results in a nearly flat tip trajectory while remaining

nearly vertically oriented (Supplementary Videos 2 and 6, and Fig. 3c, 3f). The fundamental lateral mode also exhibits a nearly flat tip trajectory due to the small passive curvature in the X direction (Fig. 3d). At high vacuum (< 0.1 mTorr), the fundamental resonance can exhibit similar displacements as in ambient conditions while requiring less than 1% of the voltage amplitude.

To verify that the beam moves at the driving frequency for the first and second order resonances, fast gating of the ICCD is used to image the beam spot over time as it traces its full period of motion (Supplementary Videos 4 and 5). Details regarding the simulated and imaged beam spots can be found in Supplementary Section 9. Because the optical signal is emitted directly from the end of a rectangular waveguide, these devices are fundamentally broadband across the visible and near-infrared spectra and can be designed for single mode or multi mode propagation. As a demonstration, Fig. 3g shows resonant beam scanning for a device operating at wavelengths ranging from 450 nm to 750 nm.

To fully characterize the frequency response (Fig. 3h), the driving frequency is swept while monitoring the X and Y displacement signals with a position sensitive photodetector (PSD). We show a peak vacuum resonant enhancement of 30 dB with mechanical quality factors exceeding 10,000, measured from ringdown (Fig. 3j). We also characterize the cryogenic compatibility of the devices by cooling the sample down to 6.9 K at high vacuum, where we observe an $\sim 2\times$ decrease in the radius of curvature. The second Y resonance shifts down to 4 kHz, and the first X resonance shifts down to 2.7 kHz. We attribute these effects primarily to differences in the coefficients of thermal expansion between the thin film layers. Frequency response measurements of a device at 6.9 K and high vacuum (Fig. 3i) demonstrate >15 dB enhancement of the first two Y resonances and first X resonance and quality factors exceeding 1000. After returning the device to room temperature, passive device curvature and frequency response returned to their pre-cryogenic state, demonstrating device stability through cryogenic cycling. See Supplementary Section 3 for experimental setup details, a full table on mechanical resonance characterization, and cryogenic cycling performance.

Two dimensional beam scanning

The combination of the 2nd order longitudinal mode and fundamental lateral mode exhibits a sufficiently flat 2D focal plane and provides a basis for achieving projection of a 2D array of diffraction-limited beam-spots for atomic control. Correction of scanning fiber displays have been demonstrated using GRIN lenses and meta-lenses and provides a path for achieving an image plane that is flat to within a single rayleigh length of the beam-spot^{13,55,67,68}.

For optimal 2D beam steering we use a device with two separate piezoelectric actuators, split down the length of the cantilever (Fig. 4a). Each electrode can be driven at multiple frequencies with different voltages and relative phases to enable the optimal excitation of both X and Y resonances simultaneously, resulting in Lissajous curves with varying refresh rates and beam-spot densities based on the exact frequency ratio^{27,69,70}. For a device with passive deflection of 85° ($L=950$ μm , $W=70$ μm), we characterize the X and Y frequency response of the device from 100 Hz to 50 kHz with dual input signals while measuring the projected beam displacement

with a PSD (Fig 4b). Driving out-of-phase signals cancels out the longitudinal response while enhancing the lateral response, allowing for cancellation of X-Y cross-coupling and the ability to drive two orthogonal axes for two-dimensional beam scanning.

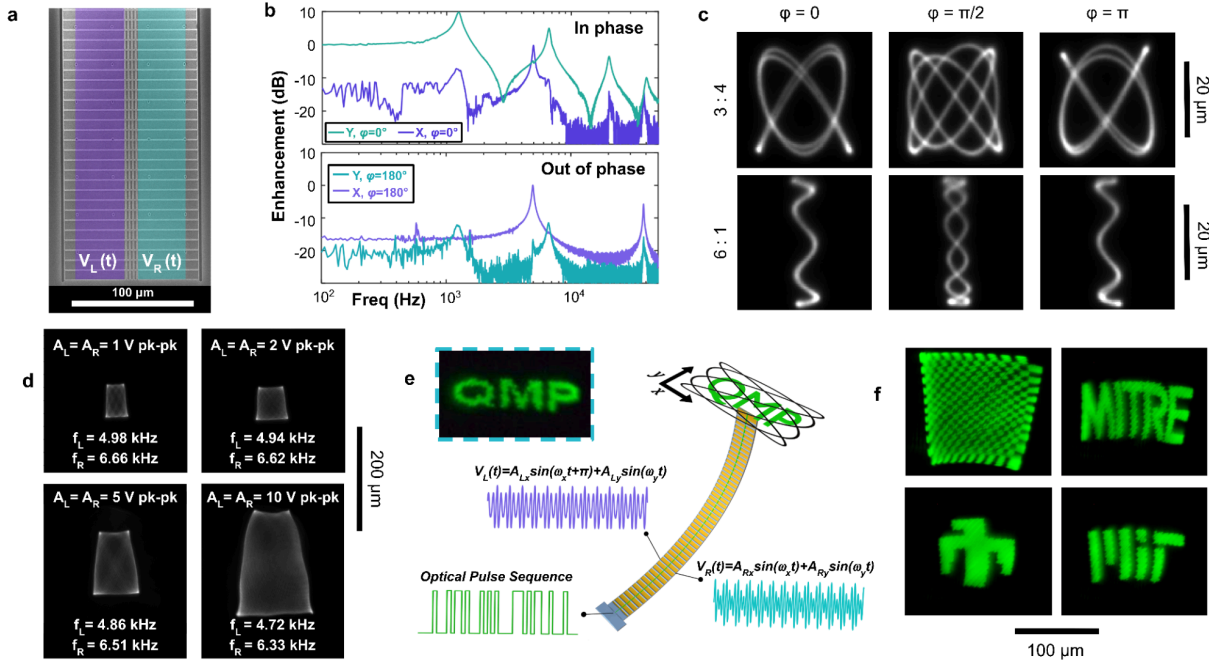


Fig. 4 | Two-dimensional beam steering with a split-electrode cantilever. **a**, Top-down SEM image of a split-electrode cantilever's base. False color added to show left (purple) and right (cyan) electrodes. **b**, Frequency response of the X and Y beam displacement. Independent voltages are applied to the left actuator [$V_L(t) = A_L \sin(2\pi f t)$] and right actuator [$V_R(t) = A_R \sin(2\pi f t + \phi)$]. The in phase dataset corresponds to $\phi = 0$ with $A_L = A_R$, and the out of phase dataset corresponds to $\phi = \pi$ with $A_L = A_R$. Out of phase measurements show high cancellation of the Y response. Data is normalized to the in phase Y displacement at low frequencies, and measurements were done in ambient conditions. **c**, ICCD images of the cantilevered waveguide's output by tracing lissajous patterns with a split-electrode cantilever driven at different frequency ratios (4.83 kHz:6.44 kHz \rightarrow 3:4 with 1.61 kHz refresh rate, and 37.2 kHz:6.2 kHz \rightarrow 6:1 with 6.2 kHz refresh rate) and different phase offsets ϕ between the X and Y drive signals. **d**, A demonstration of tuning a lissajous scan's aspect ratio by varying amplitudes A_L and A_R with the left actuator driving near 4.83 kHz and the right actuator driving near 6.5 kHz in high vacuum conditions. **e**, Diagram of arbitrary 2D image projection with a split-electrode device. Inset: an image taken of the cantilever projecting the letters "QMP" (Quantum Moonshot Project) in ambient conditions. **f**, 2D image projection examples using the split-electrode device tracing high-fill lissajous patterns in high vacuum conditions.

We generate high-rate Lissajous curves by driving signals with low relative frequency ratios at Y and X resonances simultaneously and adjusting the relative phase (Fig. 4c). By offsetting one of the frequencies, the beam will sweep across the entire 2D area (Fig. 4d). These high-fill patterns are useful for potential LiDAR and image projection applications, while high refresh rates are desirable for optical initialization and control of atomic qubits. By pulsing the optical signal of the cantilevered waveguide with an off-chip modulator, we demonstrate the projection of arbitrary 2D images using these high-fill scans (Fig. 4e-f). Modulation using on-chip modulators is readily achievable in future devices.

Ski-jump excitation of silicon vacancy color centers

s address a central goal of optically addressed qubit systems, that is, the ability to control a large number of qubits with a limited number of control channels. This is performed by

scanning the output across multiple diamond color center emitters to perform initialization and readout of their quantum state. Previous work used a controllable MZI mesh to route input laser light into four discrete channels for spatial and time-resolved control of quantum memories⁷¹. In contrast, the ski-jump has a continuous 2D range of outputs to control quantum memories as nodes on a grid. As such, the number of channels available scales based on the optical mode size exiting the waveguide and the device's range of motion.

We demonstrate this capability on a wire bonded, fiber packaged device ($L=950\ \mu\text{m}$, $W=90\ \mu\text{m}$) using 1D beam steering at ambient pressure and temperature. A diamond microchiplet consisting of 8 waveguides with implanted negatively charged SiVs is placed in a Montana 4K cryostat overhanging a bare silicon substrate (Fig 5a). Laser light resonant with the SiV zero phonon line (ZPL) around 737 nm is routed from the end of the ski-jump in free space to the tips of the individual diamond waveguides. Because an SiV may ionize to a dark neutral state and over time will cycle into an adjacent spin state, a broad 532 nm repump green laser is periodically pulsed from the side window of the cryostat onto the entire chiplet to reset the color centers into their bright state.

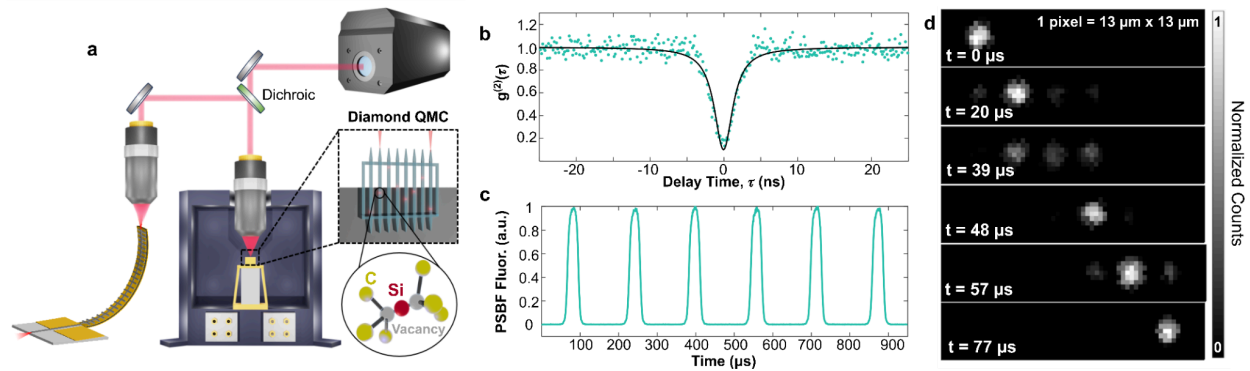


Fig. 5 | Modulation of a single photon source using resonantly driven ski-jump devices. **a**, Experimental setup for projecting the ski-jump's optical output onto a diamond quantum microchiplet with implanted SiVs and readout onto APD or ICCD. **b**, Second-order autocorrelation measurement of a single emitter in one of the diamond waveguides. $g^{(2)}(0) = 0.09(9)$, indicating that a single emitter is being addressed. The single emitter is excited by imaging the cantilevered waveguide's output. **c**, Time-dependent phonon sideband (PSB) fluorescence of the single emitter excited via the cantilevered waveguide oscillating at 6.34 kHz. The emitter is positioned at the apex of the device's range of motion. The extinction ratio is 27.5 dB with a repetition time of 157 μs . **d**, Ensemble fluorescence measurements collected with an ICCD. The driven cantilever addresses emitters in six distinct waveguides. The third waveguide, imaged at $t = 39\ \mu\text{s}$, has a damaged taper. As a result, the resonant excitation was mostly scattered.

We align the emission of the static ski-jump to one of the diamond waveguide channels and tune the excitation laser to excite the C transition of a frequency-resolved single SiV. We verify that a single emitter is being addressed by performing a second order auto-correlation measurement with $g^{(2)}(0) = 0.09(9)$, well below the 0.5 threshold for single photon emission (Fig 6b). To periodically initialize this emitter, the ski-jump is driven to oscillate at 6.34 kHz while the SiV phonon sideband (PSB) fluorescence is routed to an avalanche photodiode coupled to a time-tagger (Fig 5c). We see repeatable and consistent sideband emission with an extinction ratio of 27.5 dB, currently limited by scattered light. The standard deviation of the integrated pulse area is 0.003. We also demonstrate the control of multiple emitters in different waveguide channels by tuning the laser to a frequency that excites ensemble SiVs and scanning the

ski-jump's optical output across the channels. We collect the PSB signal from each waveguide onto a high-speed ICCD, showing their real time counts as the ski-jump sweeps over them (Fig 5d).

This chiplet has an ensemble of SiV emitters in each waveguide channel with randomly distributed ZPL frequencies. Emitters must be actively tuned into spectral alignment for future spin-photon entanglement using the ski-jump optical addressing scheme. There are existing methods to tune emitter frequencies in separate waveguides via piezoelectric⁴⁸ or capacitive⁷² strain tuning. Bulk or on-chip electro-optic modulators, such as those made from thin-film lithium niobate⁶⁴, could also be used to provide pulse carving capabilities for the ski-jump's optical signal. This would allow the ski-jump to emit optical π pulses onto individual color centers for the initialization and readout of qubit states. These modulators could also further improve the extinction ratio. Scalable control of a large number of qubits can be achieved by adapting the 2D scanning projection protocols described in the previous section to project high-speed, low fill patterns that quickly scan over an array of emitters with kHz refresh rates. Using higher order resonances, we can address emitters with a refresh rate of 40 kHz, and using a vacuum-sealed device with optimized design, we expect to use resonances over 100 kHz. Additionally, using a single ski-jump containing an array of waveguide outputs, we can perform simultaneous addressing of each diamond waveguide in a quantum microchiplet.

Discussion

We have demonstrated an actuatable out-of-plane waveguide device with a footprint of $<0.1 \text{ mm}^2$ capable of 2D beam scanning over 100,000 diffraction-limited resolvable beam spots at 737 nm, and have also demonstrated its capabilities for high extinction excitation of single SiV color centers and ensemble SiVs in separate waveguide channels. At vacuum, we show highly enhanced mechanical resonances which exhibit longitudinal deflections exceeding 250 μm at CMOS-level voltages, making encapsulation of these devices under vacuum a valuable prospect. Moreover, using the second longitudinal and first lateral resonances, we show that it is capable of projecting up to 6.8 Mspots/sec while driving both resonances simultaneously. By tiling multiple cantilevers in a 2D array, we calculate the chip area adjusted capacity as 68 Mspot/(sec* mm^2). (Supplementary Section 8).

We propose several additional paths which could improve this FoM to over 1 GSpot/(sec* mm^2). Adding corrective optics such as lenses, a spatial light modulator, and a compensation grating could improve the resolvable range of the cantilever as it bends beyond the focal plane^{13,38}. Frequency response measurements show the potential to use higher order modes exceeding 100 kHz to improve scan rates. Designing shorter cantilevers that are still capable of curling sufficiently out-of-plane should further improve the FoM by 2-4x, and a tapered cantilever design will both reduce the device size, mechanical damping and total motional mass. Moreover, by leveraging broadband and polarization maintaining propagation we can multiplex multiple wavelengths at both polarizations out of the cantilever from individual single-mode waveguides.

Finally, multiple waveguides can be embedded on a single cantilever, which will increase the emitted beams per device and could offer further improvements to the FoM by a factor of 10. In terms of pixel density, the scan rate will depend on the range at a given voltage and resonance. A tiled array covering 1 cm² can project over 110 million beam spots. Incorporating 10 waveguides/cantilever and reducing the device size from 0.1 mm² to 0.05 mm² would increase our pixel density to over 2 GSpots/cm². The combination of the capability with the existing PDK of piezo NEMS-PIC components forms the basis for a photonic engine to serve as a seamless photonic interface between a CMOS chip and the free-space world across a broad range of domains and applications.

Methods

Device fabrication and I/O

The fabrication process is similar to that laid out in Dong et al 2021⁴⁹. Cantilevers are fabricated on a CMOS platform with a silicon substrate. After an initial SiO₂ deposition, an amorphous silicon (a-Si) layer is deposited below the cantilever. The next layers are SiO₂, Al, AlN, Al, SiO₂, SiN, and lastly SiO₂. A defined etch around the cantilever exposes the underlying a-Si. Release holes are patterned every 30 um along the length and width of the cantilever to ensure a complete release from the substrate. After wafer fabrication is complete, the PICs are placed in a xenon difluoride (XeF₂) gas etching chamber which etches away the a-Si, releasing the cantilever from the substrate except for a clamp at one end. The inherent stresses in the overlying thin films, along with tailored cross-rib patterning in the top SiO₂, causes the cantilever to curl out of the PIC plane. The standard SiN waveguides used on these devices were 400 nm wide and 300 nm thick. There is an ~500 nm SiO₂ wide cladding buffer on the left and right sides of the waveguide(s), along with a top SiO₂ clad thickness of ~ 300 nm to 450 nm and a bottom SiO₂ clad thickness of ~850 nm. Pads for electrical contact use routing metal and tungsten vias to independently route signals to the top and bottom electrodes of the single electrode cantilevers. The split-electrode devices share a ground plane but use independent signal pads to control the left and right actuators. Electrical signals are sent to these pads using GSG(SG) probes or via wirebonds to a custom PCB. Laser light is routed to the ski-jumps either using an edge-coupled lensed fiber or a fully-packaged fiber-to-grating coupler system. Scanning electron micrograph images were collected using a Nanoimages SNE-4500M Plus Tabletop SEM.

Acknowledgements

Major funding for this work is provided by MITRE for the Quantum Moonshot Program. D.E. acknowledges partial support from Brookhaven National Laboratory, which is supported by the U.S. Department of Energy, Office of Basic Energy Sciences, under Contract No. DE-SC0012704 and the NSF RAISE TAQS program. M.E. performed this work, in part, with funding from the Center for Integrated Nanotechnologies, an Office of Science User Facility operated for the U.S. Department of Energy Office of Science.

Supplementary Info:

S1. Film stresses and the effect of cross-ribs on ski-jump curling behavior

Though the material stress in the SiO₂ layers is moderately compressive, the aluminum nitride (AlN) passive stress profile is a gradient from moderately compressive to moderately tensile (from bottom to top). The stresses of the Al electrodes are negligible, and the silicon nitride (SiN) stress is highly compressive. As a result, a released cantilever containing just bottom SiO₂ and Al-AlN-Al curls upward due to the combination of underlying compressive and overlaying tensile stresses. The stresses are linear, so longer and wider cantilevers will curl up to a larger final angle. Because the SiN deposited is highly compressive, increasing the thickness of the SiN or the number of SiN waveguides diminishes the cantilever's curvature. Similarly, uniformly increasing the amount of SiO₂ above the top electrode functions to reduce passive curvature. Ordinarily, this would suggest that all cladding above the top electrode should be removed aside from a small cladding buffer around the waveguides; namely, the pad open etch (POE) design.

However, if this top SiO₂ cladding is instead patterned into lateral cross-ribs rather than being removed entirely, the device curvature can be further enhanced. We qualitatively explain this phenomenon as follows: for POE devices, the material stresses are not optimally directed along the length of the cantilever to produce the desired longitudinal curvature. Rather, these devices exhibit undesired lateral curling along their width, also in part due to the concentrated compressive stress of the waveguide(s) located around the cantilever's midline. By designing devices with SiO₂ cross-ribs, lateral curvature is diminished, and the stress is more efficiently directed to enhance longitudinal curvature. The degree to which this cross-rib patterning affects device curvature can also be adjusted by changing the cross-rib period and cross-rib duty cycle. Broadly, we observed enhanced longitudinal curvature by increasing the cross-rib period and decreasing the cross-rib duty cycle. However, though the cross-ribs are useful in redirecting the material stresses, the SiO₂ is still compressive. Thus, an ideal cross-rib pattern strikes a balance between the total amount of top cladding and the periodic restraint of lateral curvature. We also note that cross-rib patterned devices were overall more uniform in their curling behavior across the wafer when compared to the POE design.

Currently, we have only fabricated devices with cross-rib periods between 1 μm and 8 μm and have not yet observed the upper bound at which this will stop enhancing longitudinal curvature. So, it is highly likely that device curvature, with accompanied shrinking of device footprint, can be improved with further optimization of the cross-rib patterning.

S2. Stroboscopic Imaging

To better understand the mechanical mode shapes of the cantilever resonances, stroboscopic imaging was used. While driving a ski-jump on one of its resonance frequencies, a fiber-coupled supercontinuum white light laser (NKT Photonics SuperK COMPACT) was pulsed at approximately the same frequency (with a slight frequency offset) and directed onto the PIC surface with a Thorlabs achromatic fiber collimator (C80APC-A, $f = 80$ mm, FC/APC, ARC: 400 - 650 nm). These stroboscopic videos were captured using a mirrorless camera (Nikon Z7 II) equipped with a macro lens (Venus Laowa 25mm, $f/2.8$, 2.5-5x). A few examples are provided as Supplementary Videos 1-3. Note that, in these videos, a set of 3 devices are being actuated with a single drive signal. These cantilevers have different widths which causes their resonance frequencies to differ. As a result, only one cantilever (nearest to the camera) is being driven directly on its resonance peak frequency.

S3. One dimensional ambient, vacuum, and cryogenic device characterization

Figure S1 shows the experimental setup for characterizing the 1D beam steering behavior of the ski-jump in Figure 3 at ambient pressure, various vacuum pressures, and cryogenic temperatures. The sample is mounted on a holder with an attached printed circuit board (PCB) and has wire bonds to ground-signal-ground (GSG) pads with an SMA feedthrough to actuate the device from DC to high frequencies (> 1 MHz). This holder is mounted on a fixed stage in a Montana CryoAdvance 100 cryostat with a nominal base temperature of 4 K. A fiber feedthrough into the cryostat allows for placement of a lensed fiber on a 3-axis stage. This enables precise edge coupling to an on-chip waveguide that routes to the ski-jump. 730 nm laser diode was used for intensified charged coupled device (ICCD) measurements, and a 532 nm Cobolt continuous wave diode pumped laser was used for position sensitive detector (PSD) measurements as it provided a sufficiently powerful optical signal.

In order to analyze control capabilities and beam quality, the optical output of the waveguide embedded on ski-jump was collected through the cryostat glass window into a 50x long working distance (LWD) objective (50X Mitutoyo Plan Apo NIR Infinity Corrected Objective, $NA = 0.42$, $WD = 17$ mm) from above. The light could then be routed a 1) CMOS camera (Thorlabs CS165CU Zelux® 1.6 MP Color CMOS Camera), 2) high-speed ICCD (Andor DH334T-18U-63), or 3) PSD (Thorlabs PDQ80A - Quadrant Detector, 400 to 1050 nm, detector bandwidth 150 kHz). The CMOS camera is primarily used to view the devices in the cryostat, align the edge-coupled fiber, and align the output of the ski-jump into the free-space optical path. A 4f system formed with two 300 mm lenses, followed by a 150 mm lens, were used to image the ski-jump output onto the ICCD. This 4f system was used to keep the beam from deviating too far from the center of the optical path during ICCD measurements. During measurements with the ICCD, the device was driven using an arbitrary waveform generator (Siglent SDG6052X),

Finally, the voltage enhancement factor was converted to decibels:

$$V_{enh,norm,dB}(f) = 10 * \log_{10}[V_{enh,norm}(f)]$$

For ambient pressure and rough vacuum, we measure the quality factor by taking the full width at half maximum (FWHM) of a Lorentzian fitted peak over each resonance's $V_{enh,norm}(f)$. At high vacuum, we see a large increase in the resonance enhancements and observe resonances up to the 150 kHz bandwidth limit of the photodetector. Here, we calculate the quality factor by monitoring the ring-down of a signal after turning off the AC input, calculating the exponential decay time constant τ and the mechanical quality factor as $Q = \pi f_0 \tau$ where f_0 is the resonance frequency.

The frequency response plots are stitched together from frequency response datasets taken at various drive voltages. To measure large enhancement at certain frequencies, the drive voltage was decreased to avoid saturation. To measure a clean response close to the noise floor, the drive voltage was increased proportionally. For both high and low voltage sweeps, data was normalized with respect to the low frequency response and stitched together to show both the noise floor and high enhancement. Table S1 details resonant frequencies, enhancements, and measured quality factors.

Table S1 Mechanical resonance characterization

Resonances	Atmospheric Pressure			Rough Vacuum (1.15 Torr)			High Vacuum (<0.1 mTorr)			Cryogenic (6.9K, <0.1 mTorr)		
	Freq (kHz)	Enh (dB)	Q	Freq (kHz)	Enh (dB)	Q	Freq (kHz)	Enh (dB)	Q	Freq (kHz)	Enh (dB)	Q
1st Y	1.16	10	5.4	1.23	15.3	24.4	1.22	30	~10000 ^a	1.28	18.1	2000 ^a
2nd Y	5.75	2.9	12.2	6.17	13	101.3	6.01	23.4	~6800 ^a	3.98	17.2	3000 ^a
3rd Y	17.98	0	14.9	18.9	10.6	246.6	18.66	16.7				
4th Y	36.31	-9.6	13.6	37.4	4.2	415.4	36.96	11.6				
1st X	3.74	-4.8	19.8	3.97	3.7	110.4	3.87	15.6	~11000 ^a	2.72	12.9	8300 ^a
2nd X	28.4	-13.7	45.3	30	-4	635.2	29.33	-0.4				

^a Q factor is measured from signal ring-down rather than FWHM.

To verify the device performance stability with cryogenic cycling, we measure the frequency response with the PSD both before and after cooling it to a cryogenic temperature of ≈ 6.9 K. Compared to room temperature, resonant frequencies were slightly shifted lower. Although the device's curling and resonant frequencies had shifted when at 6.9 K, we verified that the curling resonant frequencies and enhancement factors returned to their original values after the device returned to room temperature. Device curvature also appeared to return to its pre-cryogenic state.

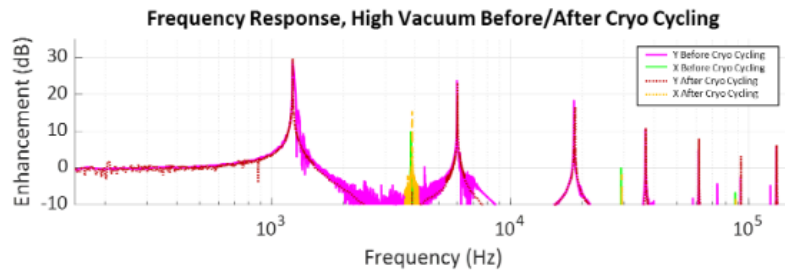


Fig. S2 | Ski-jump frequency response data at high vacuum before and after cryo cycling the device down to 6.9 K.

In order to demonstrate broadband frequency use of the ski-jump, we placed the photonic integrated circuit (PIC) on a room temperature setup similar to that used in Figure 3 but without a cryostat. A supercontinuum white light laser (NKT Photonics SuperK COMPACT) was connected to a tunable wavelength filter (SuperK Varia), providing 400 nm - 800 nm visible pulsed laser light. This optical signal was edge coupled to the PIC waveguide which routes to the ski-jump device. For the images shown in Fig. 4c, the ski-jump was driven at its second longitudinal resonance at 6.75 kHz with 40 V pk-pk. Beam streaks were collected on a Thorlabs color CMOS camera at several different wavelengths to show identical scanning ranges of ~ 40 μm under these conditions. GSG probes were placed on the GSG pads of the device to actuate it.

To observe time-resolved motion of the resonantly scanning beam, the ICCD was gated with pulses much shorter than the device's period of motion and synced with the drive signal of the cantilever. The time offset between these gate pulses and the device's drive signal was stepped up between each frame. For each acquisition/frame, many gate pulses were integrated over, with each gate occurring periodically at the device's driving frequency, to achieve sufficient counts for a clear image. An example time-resolved video for the scan shown in Fig. 3b (ambient conditions) is included as Supplementary Video 4. In this example, the ICCD was gated with 500 ns pulses with a 4 μs time step between frames.

To characterize DC actuation, DC voltages were applied to the ski-jump, and surface profile measurements of the device were obtained using an optical profilometer (Bruker ContourX-100).

S4. Two-dimensional ambient beam steering device characterization setup

Single electrode devices have AlN sandwiched between layers of Al. The split-electrode devices share a common ground plane of bottom Al metal. The top Al metal was split in half across the longitudinal midline of the cantilever, with connections to separate GSG pads sharing a common ground. This allowed for independent amplitude and phase control for each half of the device.

Fig. S3 shows the experimental setup for characterizing the split-electrode device and for demonstrating 2D beam steering with arbitrary image projection, as shown in Fig. 4 (ambient conditions). The wire-bonded sample and fiber array are each mounted on 3-axis stages to

optimize edge coupling. A lensed fiber is used to couple laser light into the PIC waveguide that routes to the ski-jump device. For data collection with the ICCD, a Hübner Photonics C-Wave GTR tunable laser set to 737 nm was used. For arbitrary image projection, a 532 nm Cobolt laser was connected to a fiber-coupled AOM to modulate the ski-jump's optical signal. To generate the necessary pulse sequence, a custom MATLAB script takes an image as an input and generates the necessary AOM pulse sequence for a given set of X and Y drive voltages and phases.

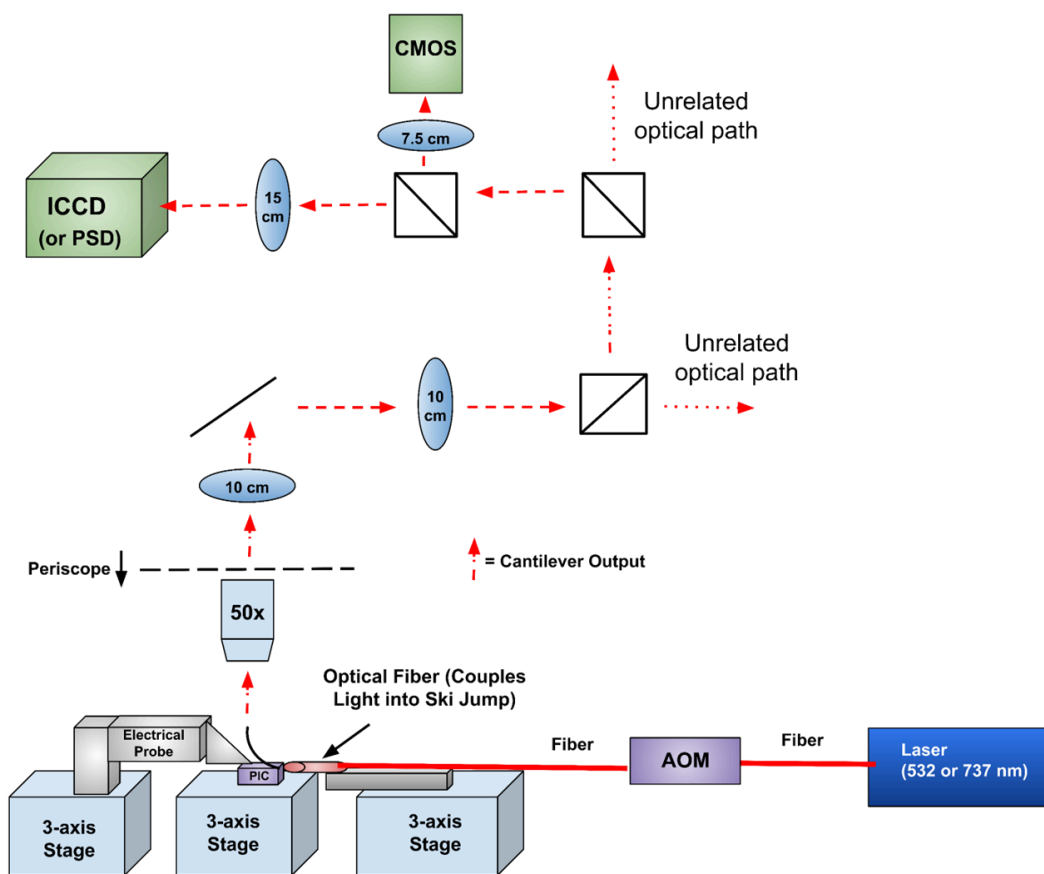


Fig. S3 | Experimental setup for characterization of two-dimensional beam steering of split-electrode device.

S5. Electrical Analysis:

The DC resistance of the device was measured with a Keithley 6487 Picoammeter, which measures the current after applying a set voltage and converts to a resistance. We measure a resistance of $> 40 \text{ G}\Omega$ with a $\pm 20 \text{ V}$ signal applied but also observe the resistance drop as the voltage amplitude and applied cantilever strain increase. At $\pm 50 \text{ V}$, we measure $\sim 1 \text{ G}\Omega$.

The AC electrical response was measured with a Keysight E5061B Impedance Analyzer. We collect the S11 response, convert to a complex impedance, and fit the imaginary portion of the

complex impedance to the equation $Im(Z) = \frac{-1}{2\pi fC}$ where f is the driving frequency and C is the capacitance. This gives a measured capacitance of 36.6 pF for a set of 3 ski-jump devices, a good match with the calculated capacitance of 30.5 pF based on the equation for a parallel plate capacitor: $C = \frac{\epsilon_0 \epsilon_r A}{d}$, where $\epsilon_0 = 8.85e-12$ F/m, $\epsilon_r = 9$ (dielectric constant for AlN), $d = 450e-9$ m, and $A = 172e-7$ m². Since this capacitance includes three devices in one test socket, the average capacitance of a single ski-jump is ~ 10.2 pF.

S6. Second Harmonic Resonances

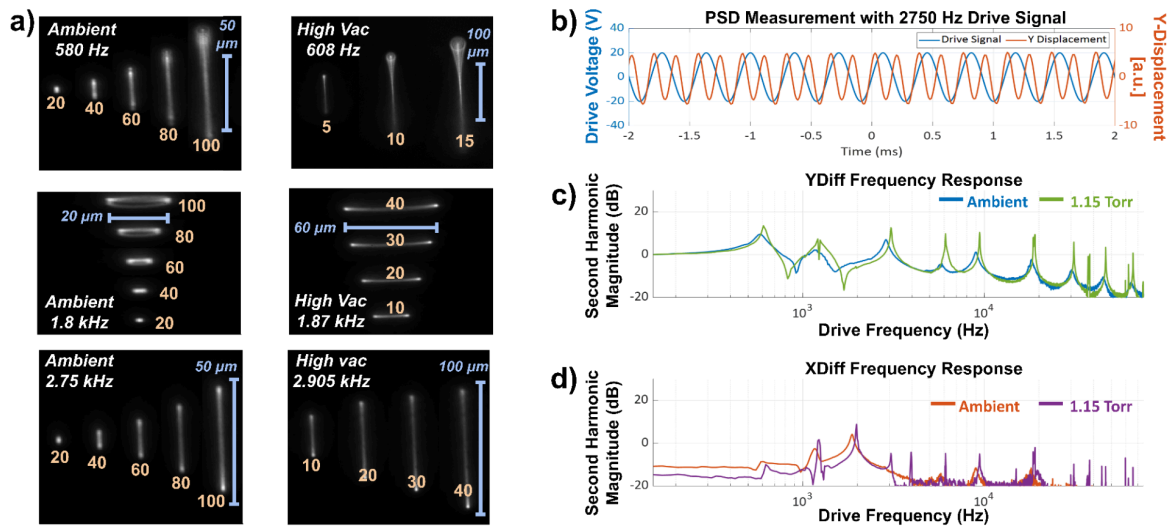


Fig. S4 | Second Harmonic Resonance data. **a)** ICCD data showing large displacement at half the resonant frequencies of certain modes. **b)** Position-sensitive detector measurement of the projected beam displacement while driving with a 2750 Hz signal, showing the displacement oscillating at 5500 Hz. **c, d)** Frequency Response Measurement from Position Sensitive Detector of the second harmonic magnitude at ambient and vacuum

Measuring the beam tip with the ICCD or the PSD, we observe several “second harmonic resonances”. In these cases, driving the cantilever at certain frequencies produces a response that shows high displacement at twice the drive frequency. These often also correspond to dips in the (fundamental) frequency response measurements. For example, driving the cantilever at 2.75 kHz while monitoring the beam tip position produces little response at 2.75 kHz but a strong response at 5.5 kHz, which also lines up with the known longitudinal mode at ~ 5.5 kHz that can be excited directly using a 5.5 kHz drive signal. This can also be seen in time-resolved imaging of the beam at this resonance in ambient conditions (Supplementary Video 5).

Comparing the second harmonic response of the longitudinal displacement shown in Fig S6c, we see a small second harmonic component of our fundamental resonances at 1.2 kHz, 5.5 kHz, and 18 kHz. However, we also observe a strong second harmonic component at half those

frequencies (around 0.6 kHz, 2.75 kHz, and 9 kHz, respectively). These frequencies did not produce a strong response at the original drive frequencies, so we note these as second harmonic resonances. Lateral displacement modes can show similar behavior, as seen in the ~ 3.6 kHz oscillation using a 1.8 kHz drive signal.

These second harmonic resonances could be a result of the strain response in the cantilever bimorph, which will have significant higher-order harmonics in the frequency domain. If these are amplified by the mechanical response of the cantilever, particularly on resonances with high enhancement, it could explain the cantilever's oscillation at twice the drive frequency.

S7. Experimental setup for ski-jump projection to diamond chiplet emitters

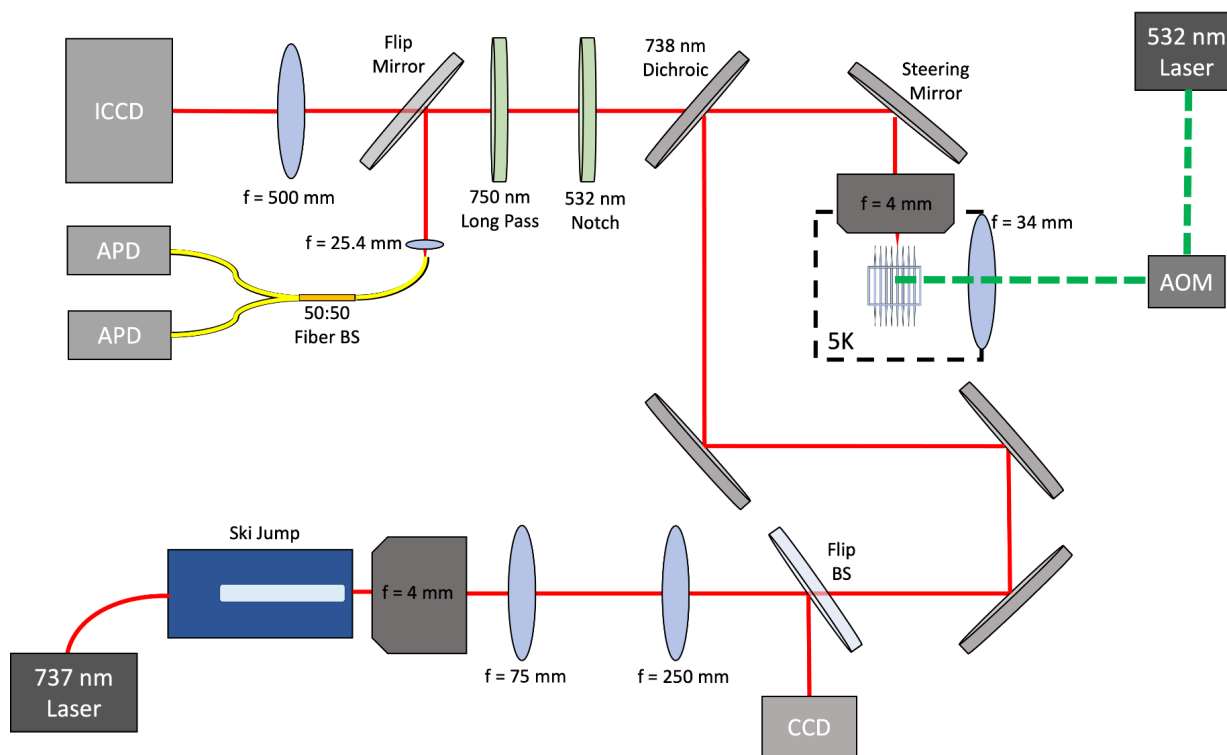


Fig. S5 | Experimental setup for ski-jump control of diamond chiplet emitters.

Fig. S5 shows the experimental setup used in the excitation of negatively charged silicon vacancy (SiV) color centers in a diamond microchiplet using a ski-jump device. Here, we used a wire-bonded, optically packaged device using a grating-coupled fiber which routes light to the ski-jump (950 μm long, 90 μm wide, 1 μm wide cross-ribs pitched at 4 μm , and a 300 nm thick x 400 nm wide SiN waveguide with a taper to a 200 nm final width at the ski-jump's tip). There are two waveguides on this device, but we only use one for qubit control in this experiment.

Tunable laser light at ~737 nm from an M Squared SolsTiS module was routed to the ski-jump using the optically packaged grating-coupled fiber. A 50x, 0.55 NA, long working distance, infinity corrected objective was used to collect the ski-jump's optical output. The optical signal was then routed in free-space to the Montana cryostat containing the diamond chiplet. A similar 50x objective was used to focus the beam onto the waveguide channels. An OBIS 532 nm laser, gated by an AOM, was focused onto the entire diamond chiplet from a side window to reset the SiV emitters as needed.

The ski-jump device was driven with an AC signal of 3.17 kHz at 100 V pk-pk. In this experiment, we took advantage of a second harmonic resonance which caused the to oscillate at 6.34 kHz with high displacement. For the time-resolved avalanche photodiode (APD) measurements (Fig. 6c), the emitter was positioned at the top of the beam streak so that the emitter would be excited once per oscillation.

SiV sideband emission was routed to a fiber-coupled APD connected to an IDQ time-tagger for high resolution time-gated measurements. For $g^{(2)}(0)$ second order auto-correlation measurements, two fiber-coupled APDs separated by a 50:50 fiber splitter were used. SiV ensemble emission from individual waveguide channels was routed to an Andor ICCD (DH334T-18F-73, 1024x1024 pixels, 13x13 um pixel size, 5 ns minimum gate width).

S8: Calculation of scan speeds and comparison to MEMS mirrors

The high vacuum ICCD measurements shown in Fig. 3b were used to calculate the pixel density, full-fill refresh rate, and beam spot capacity of our device (Fig. 1c) while driving the first X resonance at 40 V pk-pk and the first or second Y resonances at various voltages.

For 2D MEMS mirrors, the scan range, pixel density, scan speed, refresh rates, and capacity can be calculated based on the following factors: angular scanning ranges (θ_{scanX} and θ_{scanY}), angular spot sizes (θ_{spotX} and θ_{spotY}), angular drive frequencies (ω_X and ω_Y , with $\omega = 2\pi f$), and device area. Using the following equations, we calculate:

$$scan_range \text{ (\# of resolvable beam spots)} = \frac{\theta_{scanX}}{\theta_{spotX}} * \frac{\theta_{scanY}}{\theta_{spotY}}$$

$$pixel_density \text{ (beam spots/mm}^2 \text{ footprint)} = \frac{scan_range}{device_area}$$

$$scan_speed \text{ (rms beam spots/sec)} = \sqrt{\left[\frac{1}{\sqrt{2}} \frac{\theta_{scanX}}{2\theta_{spotX}} \omega_X \right]^2 + \left[\frac{1}{\sqrt{2}} \frac{\theta_{scanY}}{2\theta_{spotY}} \omega_Y \right]^2}$$

$$refresh_rate \text{ (Hz)} = scan_speed / scan_range$$

$$device_capacity \text{ (beam spots/[sec * mm}^2 \text{])} = scan_speed * refresh_rate$$

Similar metrics can be used to calculate the scan range based on the displacement of the waveguide tip, which we measure by measuring the beam streak on our ICCD (i.e. the beam's full range of motion at a resonance frequency). With this, we calculate scan range, pixel density, scan speed, refresh rates, and capacity based on the following factors: waveguide tip displacement (d_{scanX} and d_{scanY}), waveguide emitted spot size (d_{spotX} and d_{spotY}), angular drive frequencies (ω_X and ω_Y , with $\omega = 2\pi f$), and device area. Using the following equations, we calculate:

$$scan_range \text{ (\# of diffraction limited spots)} = \frac{d_{scanX}}{d_{spotX}} * \frac{d_{scanY}}{d_{spotY}}$$

$$pixel_density \text{ (beam spots/mm}^2 \text{ footprint)} = \frac{scan_range}{device_area}$$

$$scan_speed \text{ (rms beam spots/sec)} = \sqrt{\left[\frac{1}{\sqrt{2}} \frac{d_{scanX}}{2d_{spotX}} \omega_X \right]^2 + \left[\frac{1}{\sqrt{2}} \frac{d_{scanY}}{2d_{spotY}} \omega_Y \right]^2}$$

$$refresh_rate \text{ (Hz)} = scan_speed / scan_range$$

$$device_capacity \text{ (beam spots/[sec * mm}^2 \text{])} = scan_speed * refresh_rate$$

For these calculations, we use $d_{spotX} = 0.56$, $d_{spotY} = 0.42 \mu\text{m}$. We collect 2D Scan data from a split-electrode device at vacuum by measuring the 2D projection range on an ICCD Camera (Fig 5d) with various drive voltages. We use frequencies around the second longitudinal resonance (approx 6.6 kHz) and first lateral resonance (approx 4.9 kHz), but adjust the frequency to maximize the projected area. We then use the measured average X and Y displacement to calculate the scan range (in beam-spots), full-fill refresh rates (in Hz), RMS scan speed (in spots/second), and beam spot capacity (in spots/(sec-mm²)). These values are shown in Table S2.

Table S2: Calculated device scanning metrics
($d_{spotX} = 0.56$; $d_{spotY} = 0.42 \mu\text{m}$; device size=0.1 mm²)

f_X (kHz)	$V_{pk-pk X}$ (V)	d_{scanX} (μm)	f_Y (kHz)	$V_{pk-pk Y}$ (V)	d_{scanY} (μm)	2D Scan Range (spots)	Pixel Density (spots/mm ²)	Scan Speed (rms spots/sec)	Refresh Rate (Hz)	Device Capacity (spots/sec-mm ²)
4.975	1	37	6.658	1	63	9,900	99,000	2.34E6	236	2.34E7
4.938	2	52	6.615	2	60	13,064	130,640	2.32E6	177	2.32E7
4.864	5	71	6.514	5	119	35,658	356,580	4.32E6	121	4.32E7
4.720	10	106	6.333	10	196	88,074	880,740	6.85E6	78	6.85E7
4.697	30	140	6.296	30	191	113,500	1,135,000	6.86E6	60	6.86E7

We note that the refresh rate and pixel density is for a scan that maximizes the number of spots at a given drive voltage and scan range. If a lower fill factor and higher refresh rate were desired, we could increase our refresh rate while lowering the number of spots, but the scan speed and device capacity would remain approximately the same. For these metrics, we note that increasing the drive frequencies, increasing the scan range, decreasing the device area, and increasing the

number of waveguides per device are all potential ways to improve the refresh rate, pixel density, scan speeds, and device capacity.

S9: Optical mode of the cantilevered waveguide

Throughout this paper, all devices with embedded waveguides used SiN as the waveguide core with SiO₂ cladding on all sides. The waveguide core of these devices is 400 nm wide and 300 nm thick with an optional adiabatic taper to a 200 nm width at the tip. This taper was included on all devices discussed except for the broadband demonstration shown in Fig. 4c. (This was coincidental; the broadband demonstration could have also been done with a tapered waveguide.) These waveguide dimensions and materials are not fundamental to this beam scanning technology, allowing for flexibility in the optical mode design for any given application.

To image the waveguide output, an objective (50x magnification, 0.42 NA) was used to collect and collimate the light prior to refocusing onto the CMOS camera, ICCD, or PSD. In the latter case, the beam was not fully focused as the PSD requires a sufficiently large incident beam spot. We observed that the imaged beam spot size (number of pixels spanned by the beam * pixel size / optical magnification) was larger than the FEM simulations of the optical mode size. We attribute this to imperfections in the optical setup, particularly to the low NA of the objective relative to that of the ski-jump's optical mode. During vacuum and cryogenic testing, the beam also needed to pass through a thick glass window which caused further distortion of the optical mode.

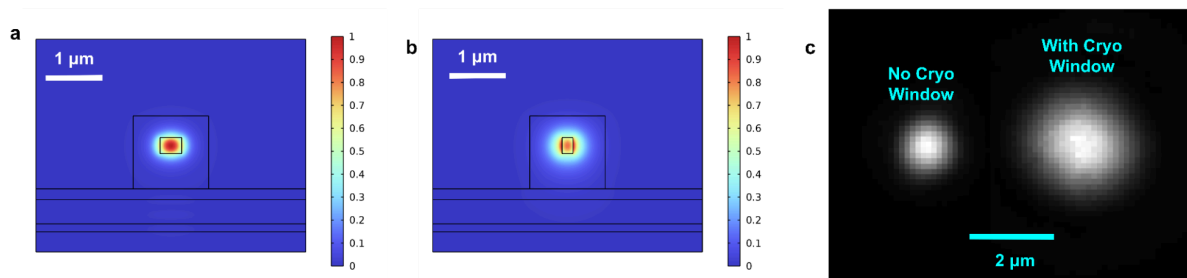


Fig. S6 | Optical output of the cantilevered waveguide. **a**, FEM simulation of the normalized electric field amplitude for the TE mode of a SiN waveguide cladded in SiO₂ operating at 737 nm. The waveguide is 400 nm wide and 300 nm thick or **b**, 200 nm wide and 300 nm thick. **c**, ICCD images of a ski-jump's TE optical output operating at 730 nm. The waveguide is 200 nm wide and 300 nm thick at the end of the cantilever. If the beam passed through the cryostat window prior to collection via the objective, the final imaged beam spot was distorted.

The simulated mode shown in Fig. S6 (a) has a mode field width of 0.56 μm and a mode field height of 0.42 μm (0.18473 μm). The simulated mode shown in Fig. S6 (b) has a mode field width of 0.66 μm and a mode field height of 0.50 μm. The imaged beam spot without passing through the cryo window had a mode field width of 1.55 μm and a mode field height of 1.64 μm. The imaged beam spot after passing through the cryo window had a mode field width of 2.99 μm and a mode field height of 2.81 μm. In these ICCD images, the ski-jump included the waveguide

taper. In Fig. S6c, the total optical magnification was 100x. The imaged mode field dimensions listed above factor out this magnification.

References:

1. Gardner, J. P. *et al.* The James Webb Space Telescope. *Space Sci. Rev.* **123**, 485–606 (2006).
2. Angel, R. Feasibility of cooling the Earth with a cloud of small spacecraft near the inner Lagrange point (L1). *Proc. Natl. Acad. Sci. U. S. A.* **103**, 17184–17189 (2006).
3. Wu, M. C., Solgaard, O. & Ford, J. E. Optical MEMS for Lightwave Communication. *J. Lightwave Technol.* **24**, 4433–4454 (2006).
4. Ishola, F. & Cho, M. Experimental study on photodiode array sensor aided MEMS fine steering mirror control for laser communication platforms. *IEEE Access* **9**, 100197–100207 (2021).
5. Lukashchuk, A. *et al.* Photonic-electronic integrated circuit-based coherent LiDAR engine. *Nat. Commun.* **15**, 3134 (2024).
6. Zhang, X., Kwon, K., Henriksson, J., Luo, J. & Wu, M. C. A large-scale microelectromechanical-systems-based silicon photonics LiDAR. *Nature* **603**, 253–258 (2022).
7. Wang, D., Watkins, C. & Xie, H. MEMS Mirrors for LiDAR: A review. *Micromachines (Basel)* **11**, (2020).
8. Awad, A., Fina, F., Goyanes, A., Gaisford, S. & Basit, A. W. 3D printing: Principles and pharmaceutical applications of selective laser sintering. *Int. J. Pharm.* **586**, 119594 (2020).
9. Ocier, C. R. *et al.* Direct laser writing of volumetric gradient index lenses and waveguides. *Light Sci Appl* **9**, 196 (2020).
10. Corsetti, S., Notaros, M., Sneh, T., Page, Z. A. & Notaros, J. Silicon-photonics-enabled chip-based 3D printer. *Light: Science & Applications* **13**, 1–11 (2024).
11. Hsiang, E.-L. *et al.* AR/VR light engines: perspectives and challenges. *Adv. Opt. Photonics* **14**, 783 (2022).
12. Xiong, J., Hsiang, E.-L., He, Z., Zhan, T. & Wu, S.-T. Augmented reality and virtual reality displays:

- emerging technologies and future perspectives. *Light Sci Appl* **10**, 216 (2021).
13. Li, Z. *et al.* Meta-optics achieves RGB-achromatic focusing for virtual reality. *Sci Adv* **7**, (2021).
 14. Packer, A. M., Roska, B. & Häusser, M. Targeting neurons and photons for optogenetics. *Nat. Neurosci.* **16**, 805–815 (2013).
 15. Demas, J. *et al.* High-speed, cortex-wide volumetric recording of neuroactivity at cellular resolution using light beads microscopy. *Nat. Methods* **18**, 1103–1111 (2021).
 16. Hamerly, R., Bernstein, L., Sludds, A., Soljačić, M. & Englund, D. Large-Scale Optical Neural Networks Based on Photoelectric Multiplication. *Phys. Rev. X* **9**, 021032 (2019).
 17. Dong, M. *et al.* Synchronous micromechanically resonant programmable photonic circuits. *Nat. Commun.* **14**, 7716 (2023).
 18. Wetzstein, G. *et al.* Inference in artificial intelligence with deep optics and photonics. *Nature* **588**, 39–47 (2020).
 19. Bernstein, L. *et al.* Single-shot optical neural network. *Sci. Adv.* **9**, eadg7904 (2023).
 20. Sludds, A. *et al.* Delocalized photonic deep learning on the internet’s edge. *Science* **378**, 270–276 (2022).
 21. Chen, Z. *et al.* Deep Learning with Coherent VCSEL Neural Networks. *arXiv [cs.ET]* (2022).
 22. Manetsch, H. J. *et al.* A tweezer array with 6100 highly coherent atomic qubits. *arXiv [quant-ph]* (2024).
 23. Menssen, A. J. *et al.* Scalable photonic integrated circuits for high-fidelity light control. *Optica* **10**, 1366–1372 (2023).
 24. Kaufmann, E. *et al.* Champion-level drone racing using deep reinforcement learning. *Nature* **620**, 982–987 (2023).
 25. Blumenthal, D. J., Heideman, R., Geuzebroek, D., Leinse, A. & Roeloffzen, C. Silicon Nitride in Silicon Photonics. *Proc. IEEE* **106**, 2209–2231 (2018).
 26. Siew, S. Y. *et al.* Review of silicon photonics technology and platform development. *J. Lightwave Technol.* **39**, 4374–4389 (2021).

27. Wang, J., Zhang, G. & You, Z. Improved sampling scheme for LiDAR in Lissajous scanning mode. *Microsyst Nanoeng* **8**, 64 (2022).
28. Hofmann, U., Janes, J. & Quenzer, H.-J. High-Q MEMS Resonators for Laser Beam Scanning Displays. *Micromachines* **3**, 509–528 (2012).
29. Li, B., Lin, Q. & Li, M. Frequency–angular resolving LiDAR using chip-scale acousto-optic beam steering. *Nature* **620**, 316–322 (2023).
30. Lin, S., Chen, Y. & Wong, Z. J. High-performance optical beam steering with nanophotonics. *Nanophotonics* **11**, 2617–2638 (2022).
31. Heck, M. J. R. Highly integrated optical phased arrays: photonic integrated circuits for optical beam shaping and beam steering. *Nanophotonics* **6**, 93–107 (2017).
32. Hofmann, U. *et al.* Resonant biaxial 7-mm MEMS mirror for omnidirectional scanning. *JM3.1* **13**, 011103 (2013).
33. Hung, A. C.-L., Lai, H. Y.-H., Lin, T.-W., Fu, S.-G. & Lu, M. S.-C. An electrostatically driven 2D micro-scanning mirror with capacitive sensing for projection display. *Sens. Actuators A Phys.* **222**, 122–129 (2015).
34. A review of physical principles and applications of acousto-optic deflectors on the basis paratellurite. *Physics & Astronomy International Journal* **3**, 62–65 (2019).
35. Pang, Y., Zhang, K. & Lang, L. Review of acousto-optic spectral systems and applications. *Frontiers in Physics* **10**, (2022).
36. Sharif Azadeh, S. *et al.* Microcantilever-integrated photonic circuits for broadband laser beam scanning. *Nat. Commun.* **14**, 2641 (2023).
37. Wang, W.-C. *et al.* Mirrorless MEMS imaging: a nonlinear vibrational approach utilizing aerosol-jetted PZT-actuated fiber MEMS scanner for microscale illumination. *Microsyst Nanoeng* **10**, 13 (2024).
38. Zhang, B., Peng, P., Paul, A. & Thompson, J. D. A scaled local gate controller for optically addressed qubits. *Optica* (2023) doi:10.1364/OPTICA.512155.

39. Bütow, J., Eismann, J. S., Sharma, V., Brandmüller, D. & Banzer, P. Generating free-space structured light with programmable integrated photonics. *Nat. Photonics* **18**, 243–249 (2024).
40. Forbes, A., de Oliveira, M. & Dennis, M. R. Structured light. *Nat. Photonics* **15**, 253–262 (2021).
41. Panuski, C. L. *et al.* A full degree-of-freedom photonic crystal spatial light modulator. *arXiv [physics.optics]* (2022).
42. Trajtenberg-Mills, S. *et al.* LNoS: Lithium Niobate on Silicon Spatial Light Modulator. *arXiv [physics.optics]* (2024).
43. Trajtenberg-Mills, S. *et al.* Metal-Optic Nanophotonic Modulators in Standard CMOS Technology. *Research Square* (2024) doi:10.21203/rs.3.rs-3606965/v1.
44. Christen, I. *et al.* An integrated photonic engine for programmable atomic control. *arXiv [quant-ph]* (2022).
45. Antonov, S., Vainer, A., Proklov, V. & Rezvov, Y. Switch multiplexer of fiber-optic channels Based on multibeam acousto-optic diffraction. *Appl. Opt.* **48**, C171–81 (2009).
46. Gooch & Housego AOD. Preprint at <https://cdn.sanity.io/files/8jt7x1sz/production/4696518084d58106722b1d5b46bc6d153d601f6e.pdf>.
47. ISOMET XY 2D AOD. Preprint at https://isomet.com/PDF%20acousto-optics_deflectors/Data%20sheets%20-%20defbluered/ODXY1441-T100S-3.pdf.
48. Clark, G. *et al.* Nanoelectromechanical Control of Spin–Photon Interfaces in a Hybrid Quantum System on Chip. *Nano Lett.* **24**, 1316–1323 (2024).
49. Dong, M. *et al.* High-speed programmable photonic circuits in a cryogenically compatible, visible–near-infrared 200 nm CMOS architecture. *Nat. Photonics* **16**, 59–65 (2021).
50. Henry Wen, Y. *et al.* High-speed photonic crystal modulator with non-volatile memory via structurally-engineered strain concentration in a piezo-MEMS platform. *arXiv [physics.optics]* (2023).
51. Dong, M. *et al.* Piezo-optomechanical cantilever modulators for VLSI visible photonics. *APL*

- Photonics* **7**, 051304 (2022).
52. Larocque, H. & Englund, D. Universal linear optics by programmable multimode interference. *Opt. Express* **29**, 38257–38267 (2021).
 53. Wen, Y. H. *et al.* Tunable Directional Couplers in a Scalable Piezo-MEMS Platform. in *Frontiers in Optics + Laser Science 2023 (FiO, LS)* (Optica Publishing Group, Washington, D.C., 2023). doi:10.1364/fio.2023.fth1e.4.
 54. Khayatzadeh, R., Civitci, F., Ferhanoglu, O. & Urey, H. Scanning fiber microdisplay: design, implementation, and comparison to MEMS mirror-based scanning displays. *Opt. Express* **26**, 5576–5590 (2018).
 55. Seibel, E. J., Johnston, R. S. & David Melville, C. A full-color scanning fiber endoscope. in *Optical Fibers and Sensors for Medical Diagnostics and Treatment Applications VI* vol. 6083 9–16 (SPIE, 2006).
 56. Liang, K. *et al.* Endoscopic forward-viewing optical coherence tomography and angiography with MHz swept source. *Opt. Lett.* **42**, 3193–3196 (2017).
 57. Frank, S., Melville, C. D., Schowengerdt, B. T. & Watson, M. D. Method and system for fiber scanning projector. *Patent* (2022).
 58. Schowengerdt, B. T. & Watson, M. D. Ultra-high resolution scanning fiber display. *World Patent* (2014).
 59. Melville, C. D., Johnston, R. S., Lee, C. M., Seibel, E. J. & Schowengerdt, B. T. Scanning laser projection display devices and methods for projecting one or more images onto a surface with light-scanning optical fiber. *US Patent* (2015).
 60. Stanfield, P. R., Leenheer, A. J., Michael, C. P., Sims, R. & Eichenfield, M. CMOS-compatible, piezo-optomechanically tunable photonics for visible wavelengths and cryogenic temperatures. *Opt. Express* **27**, 28588–28605 (2019).
 61. Larocque, H. *et al.* Programmable Multimode Interference in a VIS-NIR Photonics Platform. in *Conference on Lasers and Electro-Optics* (Optica Publishing Group, Washington, D.C., 2022).

doi:10.1364/cleo_at.2022.jth3a.50.

62. Hattori, A. *et al.* Integrated visible-light polarization rotators and splitters for atomic quantum systems. *Opt. Lett.* **49**, 1794–1797 (2024).
63. Golter, D. A. *et al.* Selective and Scalable Control of Spin Quantum Memories in a Photonic Circuit. *Nano Lett.* **23**, 7852–7858 (2023).
64. Valdez, F., Mere, V. & Mookherjea, S. 100 GHz bandwidth, 1 volt integrated electro-optic Mach–Zehnder modulator at near-IR wavelengths. *Optica* **10**, 578 (2023).
65. Timoshenko, S. Analysis of bi-metal thermostats. *J. Opt. Soc. Am.* **11**, 233 (1925).
66. Volterra, E. & Zachmanoglou, E. C. *Dynamics of Vibrations*. (C.E. Merrill Books, Columbus, Ohio, 1965).
67. Xie, N. *et al.* Large FOV short-wave infrared meta-lens for scanning fiber endoscopy. *arXiv [physics.optics]* (2022).
68. Zhang, N. *et al.* Compact piezoelectric transducer fiber scanning probe for optical coherence tomography. *Opt. Lett.* **39**, 186–188 (2014).
69. Sun, Z., Quan, R. & Solgaard, O. Resonant scanning design and control for fast spatial sampling. *Sci. Rep.* **11**, 20011 (2021).
70. Hwang, K., Seo, Y.-H., Ahn, J., Kim, P. & Jeong, K.-H. Frequency selection rule for high definition and high frame rate Lissajous scanning. *Sci. Rep.* **7**, 14075 (2017).
71. Palm, K. J. *et al.* Modular chip-integrated photonic control of artificial atoms in diamond nanostructures. *Optica* (2023) doi:10.1364/OPTICA.486361.
72. Meesala, S. *et al.* Strain engineering of the silicon-vacancy center in diamond. *Phys. Rev. B Condens. Matter* **97**, 205444 (2018).